Coastal Engineering 95 (2015) 35–50

Contents lists available at ScienceDirect

Coastal Engineering

journal homepage: www.elsevier.com/locate/coastaleng

Process-based modeling of cross-shore sandbar behavior

Benjamin Dubarbier [a,b,*], Bruno Castelle [a], Vincent Marieu [a], Gerben Ruessink [c]

[a] CNRS, UMR 5805 EPOC, 33405 Talence, France
[b] Université de Bordeaux, UMR 5805 EPOC, 33405 Talence, France
[c] Faculty of Geosciences, Utrecht University, Utrecht 3508 TC, The Netherlands

ARTICLE INFO

Article history:
Received 21 February 2014
Received in revised form 30 August 2014
Accepted 19 September 2014
Available online 30 October 2014

Keywords:
Process-based model
Velocity skewness
Acceleration skewness
On/offshore sandbar migration

ABSTRACT

A coupled wave–current–sediment transport beach profile model is used to simulate cross-shore sandbar evolution on the time scale from days to months comprising both rapid offshore and slow onshore migrations. The discrimination of four modes of sediment transport driven by velocity and acceleration skewness, mean currents and slope effects allows addressing the dominant hydrodynamic processes governing cross-shore sandbar behavior. Acceleration–skewness-induced transport systematically results in a slow onshore sandbar migration together with a slow bar growth. Velocity–skewness-induced transport can drive onshore and offshore bar migrations with substantially larger rates. Mean–current-induced sediment transport systematically drives an offshore bar migration with either bar growth or decay. Slope effects essentially act as a damping term. The water level above the sandbar crest mainly influences the sandbar migration direction, while wave obliquity regulates the magnitude of the migration rates and is crucial to accurately simulate offshore sandbar migration during energetic obliquely incident waves. The inclusion of acceleration skewness is a necessary requirement to accurately reproduce the onshore migration of shallow sandbars. Detailed inter-site comparison of best-fit model parameters shows large differences meaning that free parameters attempt to compensate some mispecifications of the physics in the model. Although this also applies to other existing beach profile models, this suggests that this model needs further improvements including, for instance, the contribution of the injection of breaking wave turbulence onto the bed to sand stirring.

© 2014 Elsevier B.V. All rights reserved.

1. Introduction

Sandbars are ubiquitous patterns along wave-exposed sandy coasts with their morphology reflecting the global state of the nearshore zone (e.g. Short, 1979; Wright and Short, 1984; Lippmann and Holman, 1990; Price and Ruessink, 2011). Nearshore sandbars provide natural protection for beaches by causing waves to dissipate away from the shoreline through depth-induced breaking, which results in lower inshore wave energy. During major storms nearshore sandbars substantially reduce the intensity of swash zone processes and potential extreme wave run-up, which is the critical component to inundation as well as dune and cliff erosion (Sallenger et al., 1985).

Sandbar behavior is one of the largest sources of morphological variability in the nearshore. During storms, intense wave breaking on the bar crest drives strong offshore-directed currents ("undertow") that transport sediment seaward, resulting in rapid (O(10 m/day)) offshore sandbar migration concurrent to erosion of the beach (e.g. Sallenger et al., 1985; Gallagher et al., 1998). During weakly to nonbreaking, yet sufficiently energetic, wave conditions the near-bed wave-nonlinearity driven bedload transport results in slow (O(1 m/day)) onshore sandbar migration concurrent with accretion of the beach (e.g. Trowbridge and Young, 1989; Gallagher et al., 1998). On the timescales of weeks, sandbars respond quasi-instantaneously to time-varying wave regimes by a rapid offshore migration or can follow a typical trend ensuing from a representative seasonal wave climate (Van Enckevort and Ruessink, 2003). On the timescales of several years, sandbars sometimes exhibit an autonomous behavior, uncorrelated with wave forcing, with sandbars describing a cyclic progressive net offshore migration (e.g. Ruessink et al., 2003b, 2009).

Several model approaches have been developed to simulate cross-shore sandbar behavior on the timescales from days to years: models based on the break point paradigm that compute sandbar migration from a wave-height dependent equilibrium location (Plant et al., 1999, 2006; Pape et al., 2010b), data-driven models based on neural networks (Pape et al., 2007, 2010a) and process-based, mostly wave phase-averaged models (e.g. Roelvink and Stive, 1989; Ruessink et al., 2007; Kuriyama, 2012; Walstra et al., 2012). The latter have recently succeeded in simulating surfzone sandbar profile evolution on timescales of days and weeks (Ruessink et al., 2007; Ruggiero et al., 2009) to years (Kuriyama, 2012; Walstra et al., 2012) with reasonable accuracy. However, a number of model limitations remain. For instance, most of the existing models ignore the contribution of acceleration skewness to the cross-shore sediment transport, although it was shown to drive a

* Corresponding author at: CNRS, UMR 5805 EPOC, 33405 Talence, France.
E-mail addresses: b.dubarbier@epoc.u-bordeaux1.fr (B. Dubarbier), B.G.Ruessink@uu.nl (G. Ruessink).

http://dx.doi.org/10.1016/j.coastaleng.2014.09.004
0378-3839/© 2014 Elsevier B.V. All rights reserved.

net onshore sediment transport (Elgar et al., 2001). A reason is that, until recently (Ruessink et al., 2012), it was unclear how to include acceleration skewness in phase-averaged beach profile models.

Overall, the respective contributions of undertow, velocity skewness, and acceleration skewness, as well as those of the different modes of sediment transport, are still not fully understood. The recent improvements in the prediction of velocity and acceleration skewness (Ruessink et al., 2012) as well as novel insights into the role of the longshore current in cross-shore sandbar behavior (Walstra et al., 2012) leave room to improve our understanding of the key processes governing cross-shore sandbar behavior.

In this paper we develop a process-based model to simulate beach profile evolution on timescales from hours to months encompassing both onshore and offshore sandbar migration events at different sites (Section 2): Duck (N.C., USA) and Egmond (The Netherlands). The new coupled phase-averaged beach profile model is presented in Section 3. The main differences with respect to previous beach profile models is the inclusion of sediment transport related to velocity and acceleration skewness using the parameterization proposed by Ruessink et al. (2012). The results are presented in Section 4 and further discussed in Section 5. We show that, using state-of-the art phase-averaged parameterizations for undertow and wave nonlinearities, cross-shore sandbar behavior is accurately simulated with low computational cost. We address the impact of the water level and the angle of wave incidence on four different modes of sediment transport, and in turn sandbar evolution, driven by velocity and acceleration skewness, mean currents and slope effects.

2. Beach profile dataset

Observations of onshore and offshore nearshore sandbar migrations at Duck (North Carolina, USA) and Egmond (The Netherlands) are used to test our beach profile model. Below we briefly describe the beach-profile evolution and corresponding hydrodynamic forcing. A more detailed overview is given in Ruessink et al. (2007).

During a selected 10-day portion of the Duck94 experiment (Fig. 1a, for extensive site and data set description see Gallagher et al., 1998), the beach exhibited a single-barred profile with the bar crest in 2-m depth and located about 100 m from the mean-sea-level shoreline. The sandbar migrated onshore about 12 m during swell waves and subsequently migrated about 20 m seaward in response to a 2-day series of high-energy waves. The beach face remained steep and featureless. During the Duck82 experiment (Fig. 1b, for extensive data set description see Trowbridge and Young, 1989), the beach exhibited a mostly single-barred profile with the bar crest in 3.5-m depth and located about 250–300 m from the mean-sea-level shoreline. During the 3.5-month period, the bar moved onshore about 65 m together with a progressive bar-trough relief reduction reaching about 50% by the end of the study period (Ruessink et al., 2007). A weakly developed inner bar was observed in about 1-m depth at mid tide. During the Egmond98 experiment, a slowly evolving double-barred beach profile was observed (Fig. 1c, for extensive site and data description see Ruessink et al., 2000). Both sandbars migrated about 30 m offshore during a 22-day series of high-energy waves with a progressive flattening of the outer bar. The inner bar displayed crescentic patterns with a cross-shore amplitude and an alongshore lengthscale of about 20 m and 600 m, respectively. Yet, during the selected forcing period, alongshore non-uniform effects on alongshore currents and on sandbar dynamics were relatively small except for the last 1–2 weeks of the Egmond98 (Ruessink et al., 2001).

3. Numerical model

In this section we describe a one-dimensional phase-averaged process-based model for sandy beach profile change on timescales of hours to months. The model is composed of 3 modules for (Section 3.1) waves, (Section 3.2) currents and (Section 3.3) sediment transport and bottom changes. The model can be coupled with a data-model assimilation module combining heterogeneous remotely-sensed video observations to inverse wave-dominated beach bathymetry (Birrien et al., 2013), which is switched off herein. We further describe (Section 3.5) the overall model set-up and (Section 3.6) the optimization method used to find the best fit free model parameters for a given field site application.

3.1. Waves

By assuming that the wave field is narrow in both frequency and direction, and neglecting bottom friction, the cross-shore (x axis) distribution of the organized wave energy, E_w, is computed using the short-wave energy flux conservation equation:

$$\frac{\partial}{\partial x}\left(E_w c_g \cos\theta\right) = -D_w, \tag{1}$$

where c_g is the wave group celerity, θ the wave angle from normal, and D_w the depth-induced breaking-wave energy dissipation. We use a modified wave-averaged bore-type analogy dissipation formulation (Battjes and Stive, 1985) to compute D_w, with the dissipation parameter $\alpha = 1$. Assuming a Rayleigh distribution of the wave height probability density function (Baldock et al., 1998) the fraction of breaking waves, Q_b, reads

$$Q_b = exp\left[-\left(\frac{H_{max}}{H_{rms}}\right)^2\right]\left(H_{max}^2 + H_{rms}^2\right) \tag{2}$$

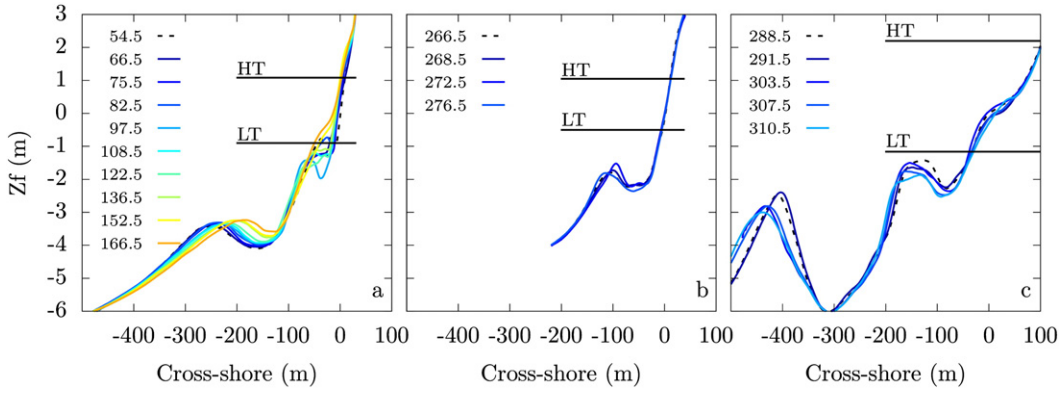

Fig. 1. Beach profiles measured during (a) Duck82, (b) Duck94 and (c) Egmond98 experiments. The initial profiles are represented in the black dashed lines and subsequent profiles are gradually colored. The lowest (LT) and highest (HT) tidal levels at each site over the considered period are represented by black lines. Numbers indicate time in Julian days.

where H_{rms} and H_{max} are the root mean square wave height and the maximum wave height for the Rayleigh probability density function, respectively. H_{max} is computed using the parameterization of the height-to-depth parameter proposed by Ruessink et al. (2003a), which reads $\gamma = 0.76k_p\overline{h} + 0.5$. Accordingly, H_{max} reads

$$H_{max} = \frac{0.88}{k_p} tanh \frac{\gamma k_p \overline{h}}{0.88}, \tag{3}$$

where k_p is the wave number related to the peak wave frequency computed with the dispersion relation using linear theory, and $\overline{h}$ is the mean local water depth.

The transfer of wave-organized energy dissipation that feeds into the roller formation is described by the roller energy flux balance equation of Dally and Brown (1995) and Nairn et al. (1990):

$$\frac{\partial}{\partial x}(2E_r c cos\theta) + D_r = D_w \tag{4}$$

where E_r is the roller energy, c is the phase velocity and $g = 9.81$ m/s^2 is the gravitational acceleration. D_r is the roller energy dissipation,

$$D_r = 2g\beta\frac{E_r}{c}, \tag{5}$$

with $\beta = 0.1$ a non-dimensional dissipation coefficients.

The wave set-up, η, is computed using the depth-integrated and depth-averaged cross-shore momentum balance equation that reads

$$\rho g\overline{h}\frac{\partial \eta}{\partial x} + \frac{\partial S_{xx}}{\partial x} + \frac{\partial S_{rx}}{\partial x} = 0, \tag{6}$$

where ρ is the water density and S_{xx} (S_{rx}) is the cross-shore wave (roller) radiation stress computed using linear wave theory.

3.2. Currents

Detailed flow measurements collected on natural beaches show that the vertical distribution of cross-shore mean currents both inside and outside the surf zone is not depth-uniform (*e.g.* Garcez-Faria et al., 2000; Reniers et al., 2004b). Outside the surf zone, boundary layer effects are important due to an enhanced eddy viscosity induced by the dissipation of short wave energy through bottom friction. This leads to an onshore directed velocity near the bottom known as the streaming effect (Henderson et al., 2004). Inside the surf zone, the depth-invariant pressure gradient induced by the wave set-up dominates the boundary layer effects, which leads to an offshore directed mean flow. This on/offshore variability of the mean flow orientation is crucial to sediment transport and, consequently, to beach profile evolution.

Accordingly, we use the quasi-1DV model formulated by Reniers et al. (2004b) which is based on the three layer conceptual model of De Vriend and Stive (1987). The model estimates analytically the vertical flow structure within the middle layer and bottom boundary layer:

$$\rho\nu_t\frac{\partial u_i}{\partial \sigma} = \frac{D_r k_i}{\omega} - F_i(1-\sigma) \qquad \text{for } \delta \le \sigma \le 1, \tag{7a}$$

$$\rho\nu_{tb}\frac{\partial u_i}{\partial \sigma} = \frac{D_r k_i}{\omega} - F_i(1-\sigma) + \frac{D_f k_i}{\omega}\left(\frac{\delta-\sigma}{\delta}\right) \qquad \text{for } 0<\sigma \le \delta, \tag{7b}$$

with k_i as the longshore and cross-shore components of the wave number k and ν_t and ν_{tb} as the vertical distribution of the turbulent eddy viscosity in the middle layer (Eq. (7a)) and the bottom boundary layer (Eq. (7b)), respectively (see Reniers et al., 2004b, for details). $\sigma = z/h$ is the scaled vertical coordinate such that $\sigma = 0$ and 1 at the bottom and at the surface, respectively. ω is the peak radial frequency, F_i is the depth-invariant forcing term composed of wave radiation stress and pressure gradients, D_f is the bottom friction dissipation, δ is the scaled bottom boundary layer width with the subscript $i = (x, y)$ standing for cross-shore or alongshore direction.

As in Ruessink et al. (2007) and Walstra et al. (2012), wave breaking is the only free surface driving force, here expressed as a shear stress, $\frac{D_r k_i}{\omega}$, and is the only source of turbulence in the middle layer as well. Within the bottom boundary layer, Eq. (7b), an additional shear stress, $\frac{D_f k_i}{\omega}\left(\frac{\delta-\sigma}{\delta}\right)$, is included to account for short-wave energy dissipation due to bottom friction, hence increasing the depth-averaged eddy viscosity. F_i in Eqs. (7a) and (7b) are unknown. These terms are determined after an integration over the water depth, which leads to the depth-averaged return current, $\overline{u}$, that compensates the onshore wave-induced mass flux (including the roller) above the wave trough level, and can be directly computed using the analytical method proposed by Reniers et al. (2004b):

$$\overline{u} = -\frac{E_w + 2E_r}{\rho c h}. \tag{8}$$

Recent laboratory observations (Reniers et al., 2004a; Dubarbier et al., 2013) reveal that the return-flow velocities tend to have their maximum shoreward of the bar crest. Accordingly, we use the breaking delay concept (Roelvink and Stive, 1989), applying a triangular weighted function on the time- and depth-averaged mean flow as in Reniers et al. (2006):

$$\overline{u}_r(x) = \frac{\int_{x-x_b}^{x}(x_b - x + x')\overline{u}(x)dx'}{\int_{x-x_b}^{x}(x_b - x + x')dx'} \tag{9}$$

where x is the local cross-shore position and $x_b = \lambda 2\pi/k_p$ is the offshore directed integration distance relative to the local wave length. The parameter λ accounts for the delay parameter which is a free coefficient in our model (as in Walstra et al., 2012). The same procedure is applied to the cross-shore distribution of the longshore mean flow. The depth-averaged and delayed mean flow is used as boundary condition to solve Eqs. ((7a) and (7b)).

In the following, the total current, $\overrightarrow{u}$, is decomposed into a mean and a wave component,

$$\overrightarrow{u}(t) = \overrightarrow{u}_\delta + \overrightarrow{\widetilde{u}}(t), \tag{10}$$

where $\overrightarrow{u}_\delta$ is the mean component obtained from Eq. (7b) after integration over the wave boundary layer, and $\overrightarrow{\widetilde{u}}(t)$ is the time varying orbital velocity specified below. Their cross-shore and alongshore components are hereafter noted $(\overline{u}_\delta, \overline{v}_\delta)$ and $(\widetilde{u}, \widetilde{v})$, respectively.

3.3. Sediment transport

Most existing phase-averaged beach profile models simulate onshore sandbar migration with fair accuracy (e.g. Ruessink et al., 2007; Walstra et al., 2012). Yet, they struggle to simulate the onshore migration of a shallow sandbar (e.g. Van Maanen et al., 2008) which can be attributed to the absence of acceleration-skewness induced transport (Hoefel and Elgar, 2003; Kuriyama, 2012). It is therefore hypothesized that acceleration-skewness induced sediment transport is crucial to onshore sandbar migration and that models ignoring this process succeed in simulating onshore bar migration through an overestimation of the velocity-skewness induced sediment transport rates. Accordingly, here we use a modified version of the Hsu et al. (2006) sediment transport formula, which discriminates the contributions of intra-wave and mean current to sediment transport, including the gravitational downslope sediment transport and the acceleration-skewness induced

transport (Hoefel and Elgar, 2003; Kuriyama, 2012). The net cross-shore sediment flux, q, is composed of the bedload transport flux, q_b, the suspended load transport q_s and acceleration-skewness induced transport, q_a:

$$q = q_b + q_s + q_a, \tag{11}$$

with

$$q_b = \rho \frac{\epsilon_b}{tan\phi}\left[\mathcal{C}_w<|\vec{\widetilde{U}}(t)|^2\widetilde{u}(t)> + \mathcal{C}_c<|\vec{U}(t)|^2 u_\delta> - \mathcal{C}_f \frac{tan\beta}{tan\phi_r}<|\vec{U}(t)|^3>\right], \tag{12}$$

$$q_s = \rho \frac{\epsilon_s}{\omega_s}\left[\mathcal{C}_w<|\vec{\widetilde{U}}(t)|^3\widetilde{u}(t)> + \mathcal{C}_c<|\vec{U}(t)|^3 u_\delta> - \mathcal{C}_f \frac{\epsilon_s tan\beta}{\omega_s}<|\vec{U}(t)|^5>\right], \tag{13}$$

where $\epsilon_b = 0.135$ and $\epsilon_s = 0.015$ are numerical coefficients (Bailard, 1981; Hsu et al., 2006), $tan\,\phi_r = 0.63$ is the tangent of internal angle of friction, $tan\beta$ is the local bed slope, w_s is the sediment fall velocity, $\mathcal{C}_w$ and $\mathcal{C}_c$ are friction coefficients related to the contributions of waves and combined waves and current, respectively, $\mathcal{C}_f$ is a gravitational friction factor and

$$q_a = -K_a(A_u A_w) \tag{14}$$

where $\mathcal{K}_a$ is a calibration coefficient, $A_w = \omega U_w$ is the near-bed acceleration amplitude with $\omega = 2\pi/T_p$ as the angular frequency, $U_w = \pi H_{rms}/\left(T_p sinh\left(k\bar{h}\right)\right)$ as the orbital velocity amplitude and A_u is the velocity asymmetry coefficient specified in Section 3.4, and H_{rms} and T_p are the root-mean-square wave height and the peak wave period respectively.

In the inner surf zone, Thornton et al. (1996) showed that the alongshore mean current can be the dominant part of the total flow during a storm event. Accordingly, Masselink et al. (2008) suggested to include the alongshore velocity as an additional sediment-stirring component in the total cross-shore flux, therefore the norm of the total velocity is used in Eqs. (12) and (13).

The sediment properties are taken into account to compute the volumetric sediment transport rate,

$$Q = \frac{q}{g(\rho_s - \rho)(1-p)}, \tag{15}$$

where ρ_s is the sediment density and $p = 0.4$ is the sediment porosity. Finally, the bed level evolution, z_b, is obtained by resolving the sediment mass conservation equation,

$$\frac{\partial z_b(t)}{\partial t} = -\frac{\partial Q}{\partial x}, \tag{16}$$

using the modified non-oscillatory central scheme of Marieu et al. (2008) to prevent from spurious bed form oscillations when there are steep peaks in the sediment transport rate.

3.4. Parameterization of velocity skewness S_u and velocity asymmetry A_s

Near-bed orbital velocity data collected in the field show, from deep to shallow water, a progressive change from a quasi-sinusoidal, to mixed skewed-asymmetric, then to strong asymmetric waveform. This is usually not fully taken into account in most of phase-averaged beach profile models (e.g. Unibest-TC Ruessink et al., 2007; Walstra et al., 2012) that only address velocity skewness. Recently, Ruessink et al. (2012) used a large field dataset to derive a parameterization of the free-stream non-linear wave orbital motion that is compatible with the analytical formulation of monochromatic intra-wave velocity proposed by Abreu et al. (2010):

$$|\vec{\widetilde{U}}(t)| = U_w f \frac{sin(\omega t) + \frac{rsin(\Phi)}{1+\sqrt{(1-r^2)}}}{1 - rcos(\omega t + \Phi)}, \tag{17}$$

where f is a dimensionless factor so that the velocity amplitude equals to U_w, r is a non-linearity parameter equivalent to an index of skewness and Φ is a waveform parameter related to the biphase. Ruessink et al. (2012) proposed a parameterization of r and Φ as a function of the local Ursell number, $U_r = \frac{3}{4}\frac{k_p H_{rms}}{\sqrt{2}\left(k\bar{h}\right)^3}$, derived from field measurements of orbital velocity skewness, $S_u = \frac{<\widetilde{u}^3(t)>}{<\widetilde{u}^2>^{3/2}}$, and velocity asymmetry, $A_u = \frac{<\left(\mathcal{H}(\widetilde{u}(t))\right)^3>}{<\widetilde{u}^2>^{3/2}}$. This method is particularly appropriated to phase-averaged wave model, as it allows estimating the cross-shore distribution of S_u, A_u, r and Φ given the modeled cross-shore distribution of H_{rms}, T_p and $\bar{h}$. The resulting parameterization differs from that derived by Kuriyama (2009) as it predicts higher skewness values in intermediate water depth and lower velocity asymmetry value in shallow water (high Ursell number).

For instance, Fig. 2 shows the modeled cross-shore distribution of S_u and A_u versus the Ursell number, together with 3 representative estimated intra-wave celerity time series. Offshore Ursell numbers correspond to the combination of the wave forcing parameters (H_{rms}, T_p, $\bar{h}$) recorded during the Duck94 experiment. For a given cross-shore position, the water level is the key factor controlling both the distribution and the intensity of S_u and A_s. For $0.01 < U_r < 0.8$ (deep water), nonlinear effects are negligible which correspond to purely sinusoidal orbital velocities. For $1 < U_r < 10$ (intermediate water depths), purely skewed to mixed skewed-asymmetric orbital velocity shapes are created. Those 3 types of waveform can be observed in the vicinity of the sandbar meaning that, across the sandbar, the respective magnitude of acceleration skewness and velocity skewness is highly variable depending on the wave and tide conditions. Interestingly enough, purely asymmetric orbital velocities, corresponding to the dominance of bores, are systematically found near the shoreline in shallow water condition ($U_r > 10$), that is in the inner surf zone.

3.5. Model set-up

A regular grid is considered for all the simulations. The grid cell size is $\Delta x = 2$ m, and the grid origin, $x = 0$, is situated at the mean-sea-level shoreline ($z = 0$). The cross-shore orientation is defined as positive in the onshore direction. The offshore boundary of the model is located at the offshore wave sensor that is, for Duck $x = -600$ m in about 7-m depth and for Egmond at $x = -1800$ m in about 15-m depth. The collected wave-forcing time series (H_{rms}, T_p, θ) and tidal elevation are interpolated every 30 min for each site. The angle of wave incidence was not measured during Duck82 experiment. Given that waves were observed to have an essentially shore-normal incidence (Trowbridge and Young, 1989), shore-normal incidence is therefore applied as in previous Duck82 modeling (Ruessink et al., 2007). For Egmond, a constant median grain sizes of 180 μm is applied while two different median grain size are used for Duck, in order to simulate the bi-modal cross-shore distribution observed at this site. A fine grain size (170 μm) was applied in the lower part of the profile (for $\bar{h} \geq 1.5$), and a coarser grain size (400 μm) in the intertidal and upper part. Following Ruessink et al. (2007), the bed level changes were computed from the offshore boundary to the location where the relative peak period, $T_p\sqrt{\frac{g}{h}}$, exceeds 40 for the first time, in order to exclude the swash zone, where our sediment transport approach is not appropriate. This threshold value is kept constant for all simulations. However, for steep beachface this sediment transport cut-off results in unrealistic sediment transport due to an overestimation of the undertow that can ultimately

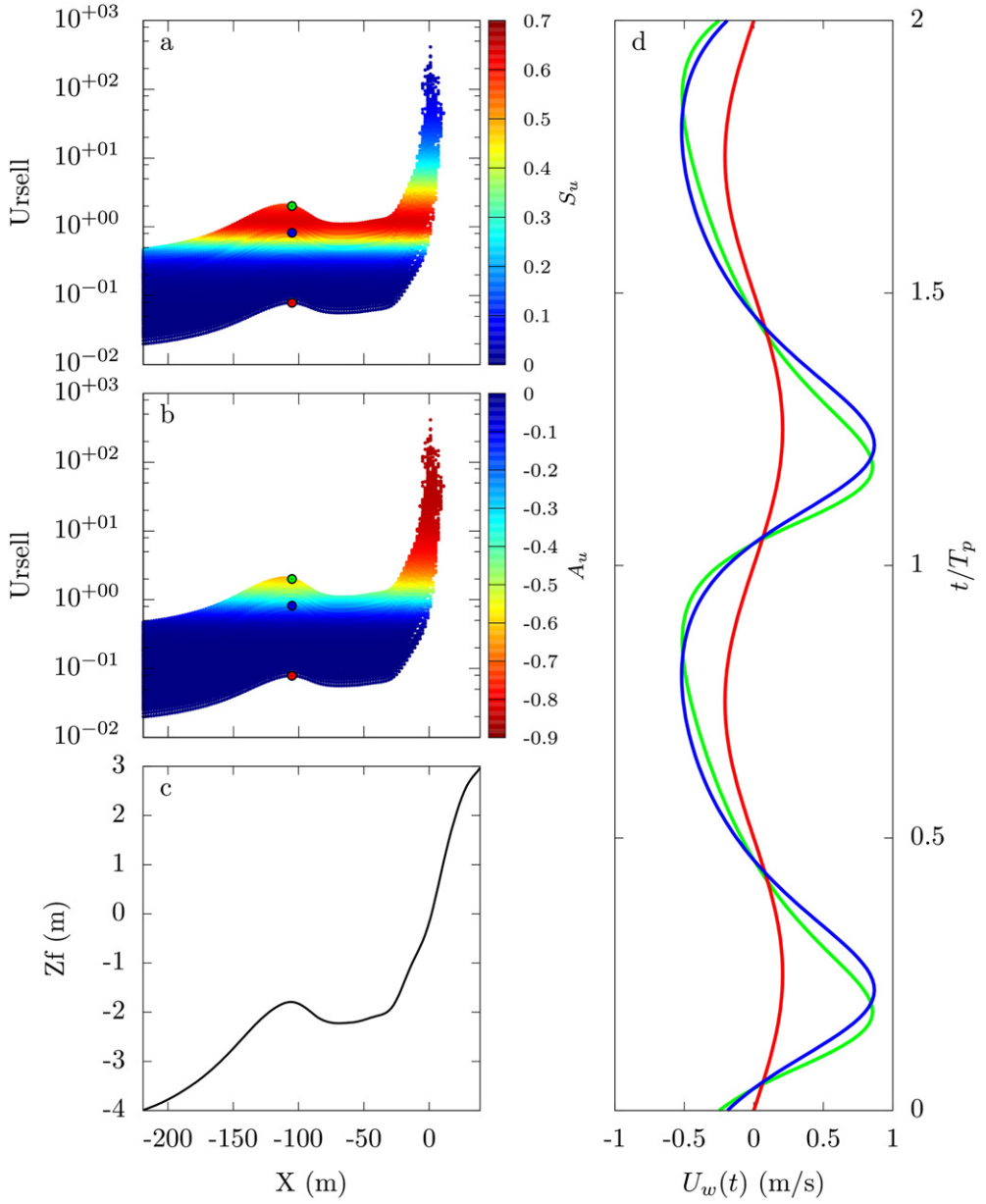

Fig. 2. Simulated (a) velocity skewness S_u and (b) velocity asymmetry A_u estimated from Duck94 forcing time series as a function of both the cross-shore position and Ursell number, (c) the initial Duck94 profile and (d) time series of near-bed orbital velocity corresponding to representative zones indicated by the corresponding colored dots in (a,b). The red dot refers to a region of zero velocity skewness, the blue dot to purely skewed orbital velocity and the green dot to mixed skewed-asymmetric orbital velocity.

create spikes in the upper part of the profile. For each beach study, preliminary model runs are used via optimization to find the shortest distance from the cross-shore position where the condition on the relative peak period is satisfied in order to avoid unrealistic profile evolution.

3.6. Optimization method

The model is characterized by a number of calibration parameters. The friction coefficients, $\mathcal{C}_w$, $\mathcal{C}_c$, $\mathcal{C}_f$, and $\mathcal{K}_a$, together with the delay parameter, λ, are the free parameters, all the other parameters being set to values typically found in the literature (Gallagher et al., 1998; Ruessink et al., 2003a; Reniers et al., 2004b; Ruessink et al., 2012). Each friction coefficient is related to a typical sediment transport mode that drives a given sandbar behavior that will be discussed later in the paper. The delay parameter also impacts the sandbar behavior as it determines the onshore-shift of the maximum return flow. These free parameters are independent (Ruessink, 2005), which allows them to be the variables of a non-linear optimization problem. For each field site application, the corresponding calibration parameters are found using a simulated annealing algorithm (Bertsimas and Tsitsiklis, 1993), by minimizing the cost function,

$$F(p) = \sum_{x_c, t^{obs}} \left(z_b^{model}\left(x_c, t^{obs}|p\right) - z_b^{obs}\left(x_c, t^{obs}\right)\right)^2, \quad (18)$$

where p indicates a random combination of the free parameters, x_c the cross-shore zone where the optimization is performed, t^{obs} the times when observations are available, z_b^{model} (z_b^{obs}) the simulated (measured) bed level. This cost function is particularly adapted to the optimization method as it minimizes the cumulative squared difference between modeled and observed profiles. The simulated annealing algorithm is slow to reach convergence and needs a large amount of trials to reach the global minimum of a system. Parallelization architecture was used

Table 1
Synthesis of optimized parameters for each field site.

Site	$\mathcal{C}_w$	$\mathcal{C}_c$	$\mathcal{C}_f$	$\mathcal{K}_a$	λ
Duck82	0.00320	0.00913	0.02996	$0.188. \times 10^{-4}$	4.9
Duck94	0.00483	0.02002	0.01173	$0.631. \times 10^{-4}$	1.57
Egmond98	$4. \times 10^{-7}$	0.00228	0.00256	$0.01. \times 10^{-4}$	4.9
Duck94: $\overline{V_\delta}$ switched off	0.0000077	0.02999	0.01127	$1.1. \times 10^{-4}$	2.15
Duck94: $Q_{\mathcal{K}_a}$ switched off	0.01235	0.02243	0.03628	0.0	3.2

in order to increase the number of trials in the same elapse time of a sequential procedure. For each numerical experiment the searching algorithm is trained over a minimum of 10^4 trials, covering an extended searching-space of documented values for each free parameter ($1.e^{-6} \leq \mathcal{C}_w \leq 3.e^{-2}$, $1.e^{-6} \leq \mathcal{C}_w \leq 3.e^{-2}$, $1.e^{-6} \leq \mathcal{C}_f \leq 3.e^{-2}$, $1.e^{-8} \leq \mathcal{K}_a \leq 2.5e^{-4}$ and $0.5 \leq \lambda \leq 5.0$). The cross-shore domain boundaries used in each optimization procedure correspond to $-400 \leq X \leq -100$ m for Duck82, $-150 \leq X \leq -50$ m for Duck94 and $-300 \leq X \leq -30$ m for Egmond98.

4. Model results

Table 1 gives the free parameters obtained with the optimization method performed for each experiment described in Section 2. The Brier skill score is used as an index of model performance relative to a baseline prediction of no change from the initial profile (Van Rijn et al., 2003):

$$Skill\left(t^{obs}\right) = 1 - \frac{\sum_{x_c}\left(z_b^{\text{model}}\left(x_c, t^{\text{obs}}|p\right) - z_b^{\text{obs}}\left(x_c, t^{\text{obs}}\right)\right)^2}{\sum_{x_c}\left(z_b^{\text{obs}}\left(x_c, t^{\text{obs}}\right) - z_b^{\text{obs}}\left(x_c, t^{\text{obs}} = t_0\right)\right)^2} \quad (19)$$

Positive, zero, or negative values indicate that the model prediction is better, equal, or worse than the baseline prediction of no change. In the following we describe separately (Section 4.1) the simulated morphological evolutions for the 3 experiments and (Section 4.2) the underlying physical processes governing sandbar behavior, focusing on the Duck94 experiment.

4.1. Morphological evolution

Figs. 3, 4 and 5 show the model results for Duck82, Duck94 and Egmond, respectively. Fig. 6 focuses on specific snapshots of the simulated and measured bed profile evolution, for the three experiments. The model successfully simulates (1) the slow onshore migration rates of 0.45 m·day^{-1} for Duck82 (Fig. 3) and 1.3 m·day^{-1} for Duck94 (Fig. 4) and (2) the slow 1.37 m·day^{-1} and rapid

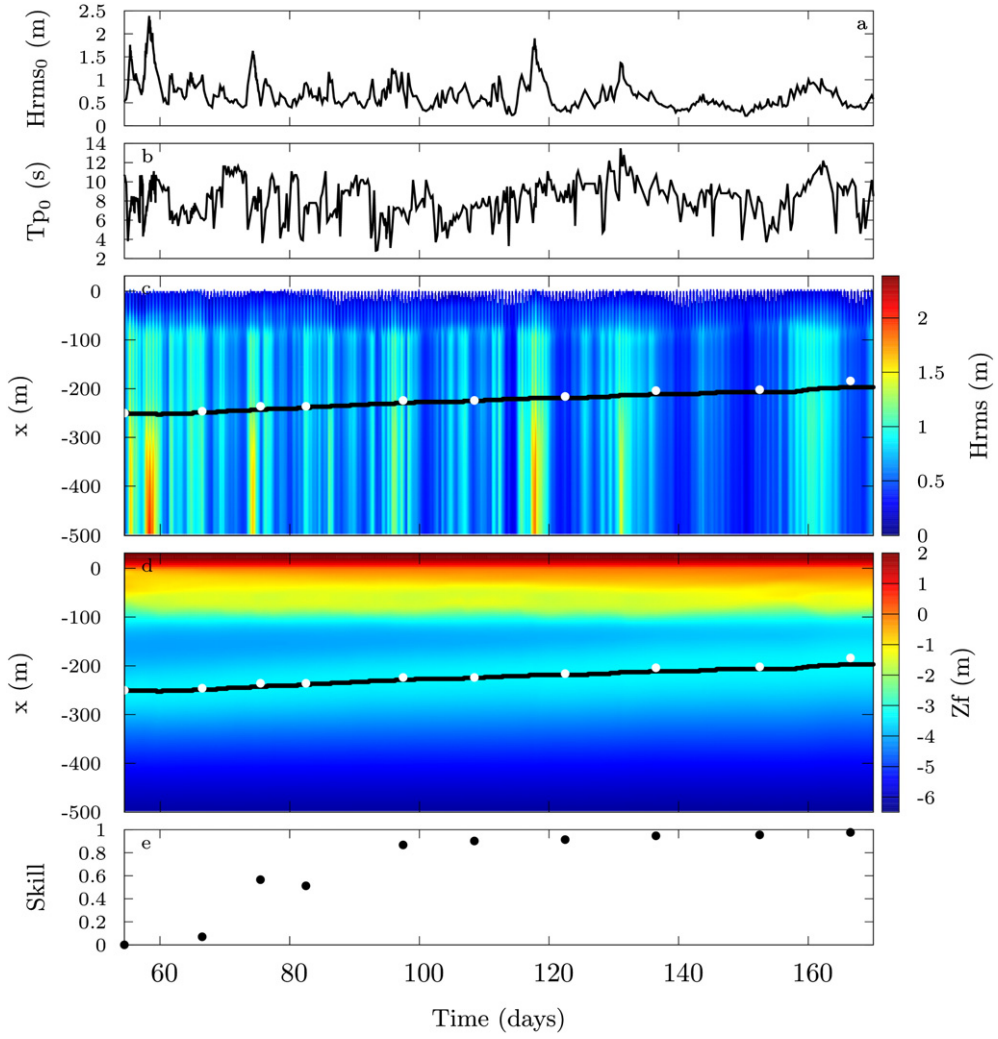

Fig. 3. Simulation of Duck82 beach profile evolution using the optimized quintuplet free parameters. Offshore measured time series of (a) root mean square wave height and (b) peak wave period. Time–space diagram of simulated (c) H_{rms} and (d) bottom elevation with (e) corresponding Brier skill parameter calculated over the optimized zone. The black line (white dots) indicates the simulated (measured) sandbar crest position.

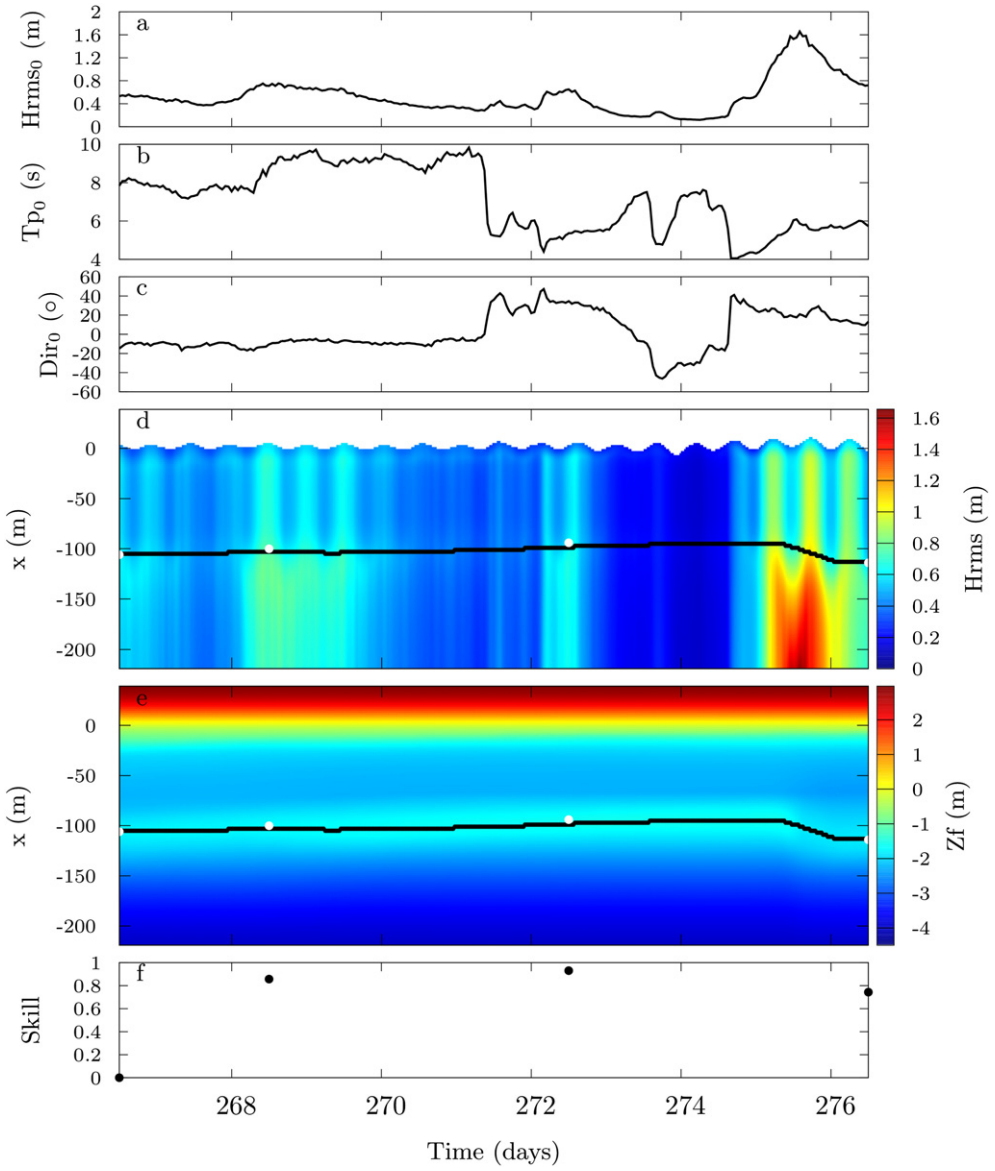

Fig. 4. Simulation of Duck94 beach profile evolution using the optimized quintuplet free parameters. Offshore measured time series of (a) root mean square wave height, (b) peak wave period and (c) mean wave angle. Time–space diagram of simulated (d) H_{rms} and (e) bottom elevation with (f) corresponding Brier skill parameter calculated over the optimized zone. The black line (white dots) indicates the simulated (measured) sandbar crest position.

37.5 m·day^{-1} offshore migration rates during Egmond98 (outer-bar) and Duck94, respectively. The simulation of the prolonged onshore sandbar migration during Duck82 reproduces the bar-trough relief reduction about 50% (Fig. 6a–c). Yet, the model does not simulate the observed upper-profile accurately (-100 m $< x < -10$ m), as a small terrace feature is formed. However, its offshore extent is less pronounced than for the same simulation in Fig. 8 g–i of Ruessink et al. (2007).

Unlike previous non-coupled (Hoefel and Elgar, 2003; Henderson et al., 2004; Hsu et al., 2006) and coupled (Ruessink et al., 2007) morphodynamic model efforts, the onshore sandbar migration during Duck94 is reproduced accurately with a skill index about 0.93 at the end of the sequence ($t = 272.5$ days) (Fig. 4f). Unlike the sandbar shape evolution during Duck82, during Duck94 the bar grows and tends to have an asymmetric shape with a steep shoreward flank and a pronounced trough that are well captured by the model (Fig. 6d–e). Despite a skill index dropping to 0.5, the model is able to reproduce the sandbar offshore migration during the energetic event, accompanied by a very steep seaward flank.

The simulation on Egmond98 shows similar model performance to that in Ruessink et al. (2007). The model reproduces a quasi-steady offshore migration of both bars (Fig. 5e), with a decreasing outer bar-trough amplitude (Fig. 5f–h). At the beginning of the experiment, the model underestimates the offshore migration of the outer bar (see Fig. 6g) resulting in a negative skill index. The rest of the simulation shows a good model performance, especially for the outer bar with a skill index higher than 0.7 at the end of the simulation (Fig. 5f). Similar to Ruessink et al. (2007) and Van Rijn et al. (2003), the largest differences between the model and the measurements are found for the inner-bar evolution as the model overestimates the bar amplitude, resulting in an inner-bar skill index of 0.3 at the end of the simulation (Fig. 5f). The decreasing model performance is attributed to the observed change from an alongshore-

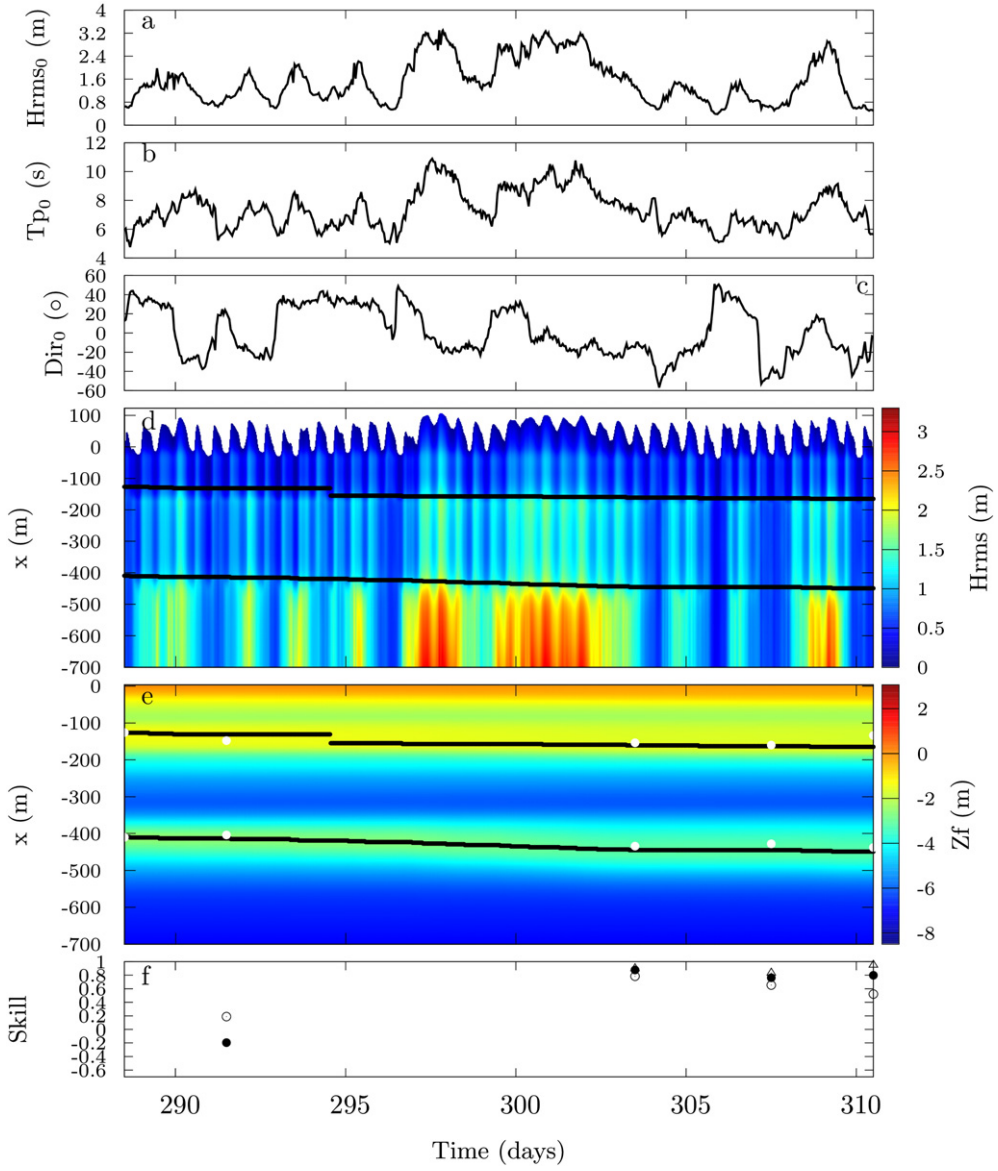

Fig. 5. Simulation of Egmond98 beach profile evolution using the optimized quintuplet free parameters. Offshore measured time series of (a) root mean square wave height, (b) peak wave period and (c) mean wave angle. Time–space diagram of simulated (d) H_{rms} and (e) bottom elevation with (f) corresponding Brier skill parameter calculated over the entire profile (black dots) and inner-bar (white dots). The black lines (white dots) indicate the simulated (measured) sandbar crest positions.

uniform to a quasi-rhythmic inner-bar morphology (Ruessink et al., 2000).

4.2. Underlying physical processes

Here we focus on the Duck94 simulation to further analyze the underlying physical processes governing onshore and offshore sandbar migrations. The time evolution of the cross-shore distribution of the hydrodynamics (Fig. 4) and that of the sediment transport (Fig. 8) are contrasting in pattern for the three different wave conditions: (1) low-energy swell regime (t = 266.5–271 days), (2) low-energy wind–wave regime (t = 271–274.5 days) and (3) an energetic wind–wave regime (t = 274.5–276.5 days).

Fig. 7 shows the time–space evolution of the hydrodynamics. During the first stage of the first wave regime, the sandbar crest does not migrate due to mostly non-breaking wave conditions across the bar. Wave energy dissipation rate subsequently increases up to 40 $N \cdot m^{-1} \cdot s^{-1}$ during low tides (t = 268–271 days, Fig. 7a), which initiates a slow onshore sandbar migration. During the more energetic seas (t = 274.5–276.5 days), the dissipation rate increases up to 140 $N \cdot m^{-1} \cdot s^{-1}$, which is associated with a rapid offshore migration of the sandbar.

Short-wave flow moments result from the near-bed velocity skewness S_u and asymmetry A_u parameterization. Interestingly enough, both S_u and A_u clearly change in pattern between swell ($T_p > 6s$) and sea-wave ($T_p \leq 6s$) regimes (Fig. 7b,c). During the swell regime (t = 266.5–271 days), large skewness (S_u = 0.5–0.6) and asymmetry ($A_u = -0.5 - -0.6$) values dominate most of the surfzone region. At high tide, maximum skewness and asymmetry occur near and shoreward of the bar crest, respectively. In contrast, at low tide, maximum skewness (asymmetry) is located seaward of (at) the bar crest. During the wind–wave regime, high S_u and A_u values are centered at the sandbar crest with tide modulating the magnitude. Large skewness and asymmetry values are also systematically found in

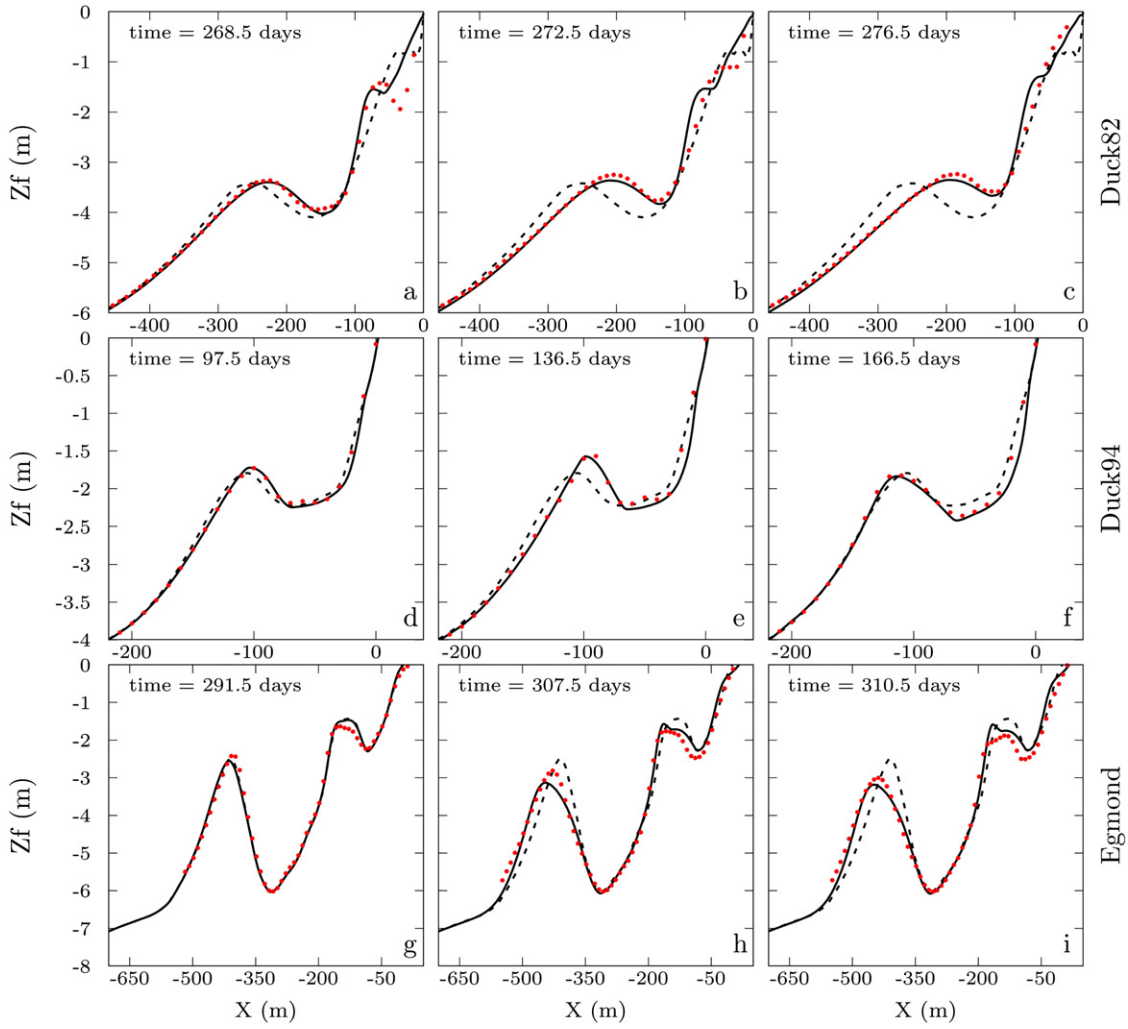

Fig. 6. Evolution of the measured (red dots) and modelled (solid line) cross-shore bed elevation for (a–c) Duck82, (d–f) Duck94, (g–i) Egmond98 experiments. The initial profile is represented by the dashed line.

the inner surf zone near the shoreline. The corresponding short wave odd flow moments $<|\widetilde{\vec{U}}(t)|^2\widetilde{u}(t)>$ (noted $<|u_{nl}|^2u_{nl}>$ in Ruessink et al. (2007)) and $<|\widetilde{\vec{U}}(t)|^3\widetilde{u}(t)>$ related to short-wave induce bedload and suspended-load, respectively, are of comparable magnitude (not shown). The former component ranges from 0 to 0.2 m^3/s^3 in agreement with Hsu et al. (2006) and Ruessink et al. (2007), and $<|\widetilde{\vec{U}}(t)|^3\widetilde{u}(t)>$ ranges from 0 to 0.35 m^4/s^4.

The simulated mean return flows (Fig. 7d) are very similar in pattern to those simulated in Ruessink et al. (2007) on exactly the same benchmark. Although this is a good validation test case, this is not surprising given the similarities in our wave and undertow models with those of Ruessink et al. (2007). Of note, for significant depth-induced breaking wave energy dissipation, the seaward flow magnitude at the top boundary is about 30% larger than the depth-integrated mean return flow. Both offshore and in the vicinity of the sandbar crest, U_δ is onshore directed, reflecting a shoreward mean Eulerian streaming flow occurring in the boundary layer with a maximum velocity of 9 cm/s. The time-averaged and depth-integrated alongshore current V_δ reaches 1.2 m/s near the bar crest during the high energy seas (t = 275.5 days, Fig. 7e), which is consistent with the values reported by Gallagher et al. (1998).

To further address the primary sediment transport processes driving cross-shore sandbar migration, we split the net sediment transport into four modes related to short-wave skewness ($Q_{\mathcal{C}w}$) and asymmetry ($Q_{\mathcal{K}a}$), mean currents ($Q_{\mathcal{C}c}$) and slope effect ($Q_{\mathcal{C}f}$):

$$\begin{aligned} Q_{\mathcal{C}_w} &= \mathcal{C}_w\left[\rho\frac{\epsilon_b}{tan\phi}<|\widetilde{\vec{U}}(t)|^2\widetilde{u}(t)> + \rho\frac{\epsilon_s}{\omega_s}<\left|\widetilde{\vec{U}}(t)\right|^3\widetilde{u}(t)>\right] \\ Q_{\mathcal{C}_c} &= \mathcal{C}_c\left[\rho\frac{\epsilon_b}{tan\phi}<|\vec{U}(t)|^2u_\delta> + \rho\frac{\epsilon_s}{\omega_s}<|\vec{U}(t)|^3u_\delta>\right] \\ Q_{\mathcal{C}_f} &= \mathcal{C}_f\left[\rho\frac{\epsilon_b tan\beta}{tan\phi^2}<|\vec{U}(t)|^3> + \rho\frac{\epsilon_s^2 tan\beta}{\omega_s^2}<|\vec{U}(t)|^5>\right] \end{aligned} \quad (21)$$

the term $Q_{\mathcal{K}a}$ is given by Eq. (14) in Section. 3.3. During the low-energy swell period, the net sediment transport (Fig. 8e) is onshore directed mostly because of the contribution of $Q_{\mathcal{C}w}$ (Fig. 8a). The latter is systematically onshore directed, with maximum magnitude near the sand bar crest, and notably extend farther offshore during the high-energy seas (t = 274.5–276.5 days in Fig. 8a). $Q_{\mathcal{K}a}$ also contributes to the total onshore sediment transport with maximum flux located, for all three wave conditions, in the vicinity of the sandbar crest and over the upper profile. Clearly, the cross-shore gradients in net sediment fluxes result in the progressive slow onshore sandbar migration (Fig. 8e). Similar patterns were simulated for Duck82 with an additional important contribution of $Q_{\mathcal{C}f}$ to reproduce the 50% reduction in bar-trough relief. Offshore

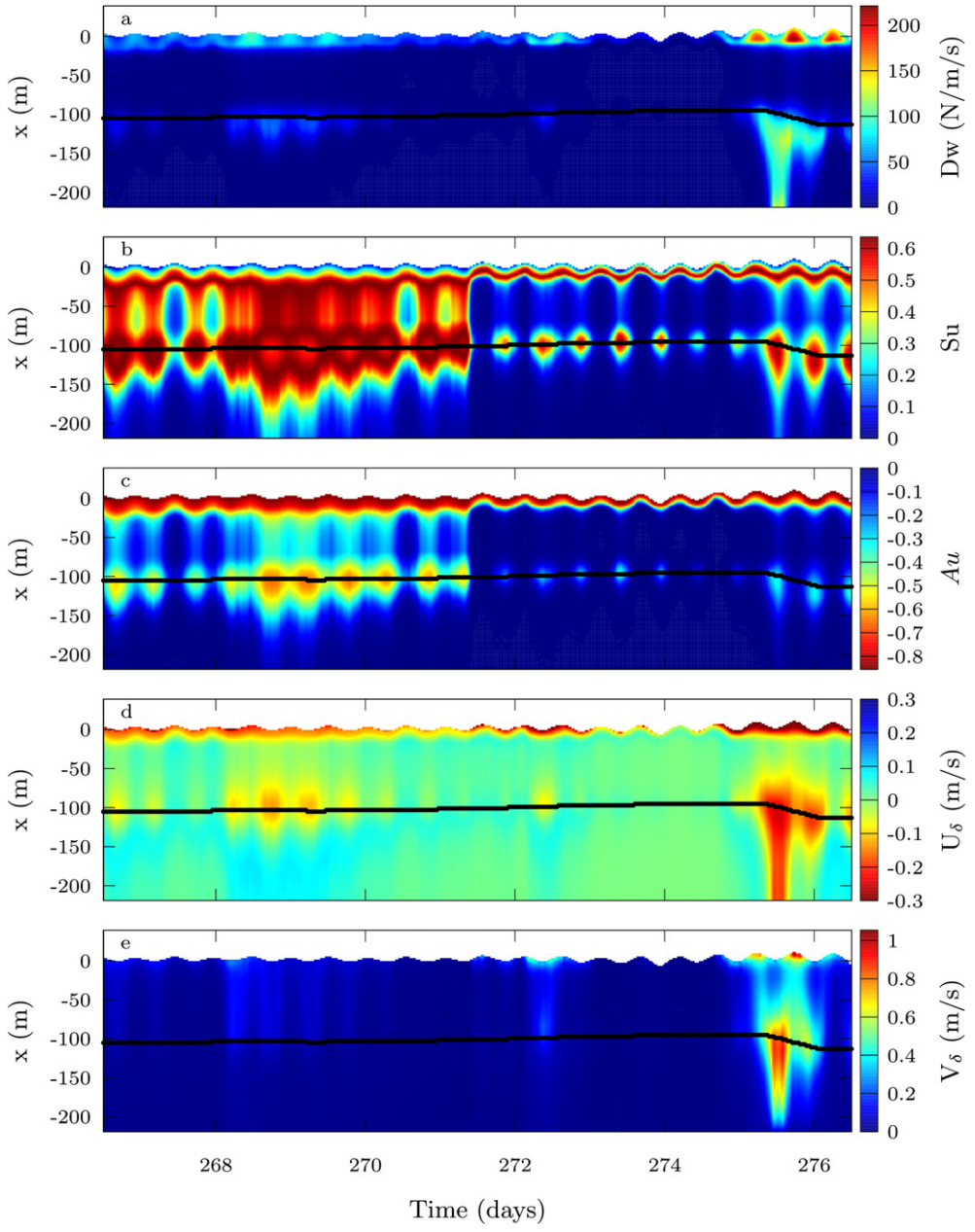

Fig. 7. Time–space diagram of simulated (a) wave dissipation, (b) velocity skewness, (c) acceleration skewness, (d) top boundary layer cross-shore mean current U_δ and (e) top boundary layer alongshore mean current V_δ for the Duck94 experiment. The superimposed dark line indicates the simulated sandbar crest positions.

of the bar crest, $Q_{\mathcal{C}c}$ is also onshore directed due to streaming effects (Fig. 8b,e). This is in line with the study of Henderson et al. (2004), see for instance Fig. 6a. Simulations show that this onshore streaming-related transport is of secondary importance for onshore sandbar migration compared to the contribution of the near-bed wave non-linearity.

Periods of low wave-energy dissipation across the sandbar result in zero sediment transport with the sandbar remaining at the same location ($t = 271$–274.5 days). At the end of the simulation during the energetic wave conditions the net sediment is essentially offshore directed and about 10 times larger in magnitude than the maximum onshore flux simulated over the entire simulation. The resulting cross-shore gradients in $Q_{\mathcal{C}c}$ move the sandbar crest by 30 m offshore. At Egmond, offshore migration of the outer bar is also found to be controlled by $Q_{\mathcal{C}c}$ (not shown).

5. Discussion

5.1. Parameter values

Similar to previous process-based beach profile models (Ruessink et al., 2007; Kuriyama, 2012; Walstra et al., 2012), a number of free model parameters required calibration through optimization operations. As can be deduced from Table 1, optimum $\mathcal{C}_w$, $\mathcal{C}_c$, $\mathcal{C}_f$ and $\mathcal{K}_a$ vary between sites and campaigns. The delay parameter λ, which is crucial to sandbar migration as it controls the onshore-shift of the maximum return flow is systematically larger than 3. For the Duck82 and Egmond98 experiments, λ reaches the upper limit of 5. Between Duck82 and Duck94 experiments, both $\mathcal{K}_a$ and $\mathcal{C}_f$ vary by a factor 3, $\mathcal{C}_c$ by a factor 2 and $\mathcal{C}_w$ by a factor <2. For the Egmond98 experiment, coefficients $\mathcal{C}_w$ and $\mathcal{K}_a$ are much smaller than for the Duck

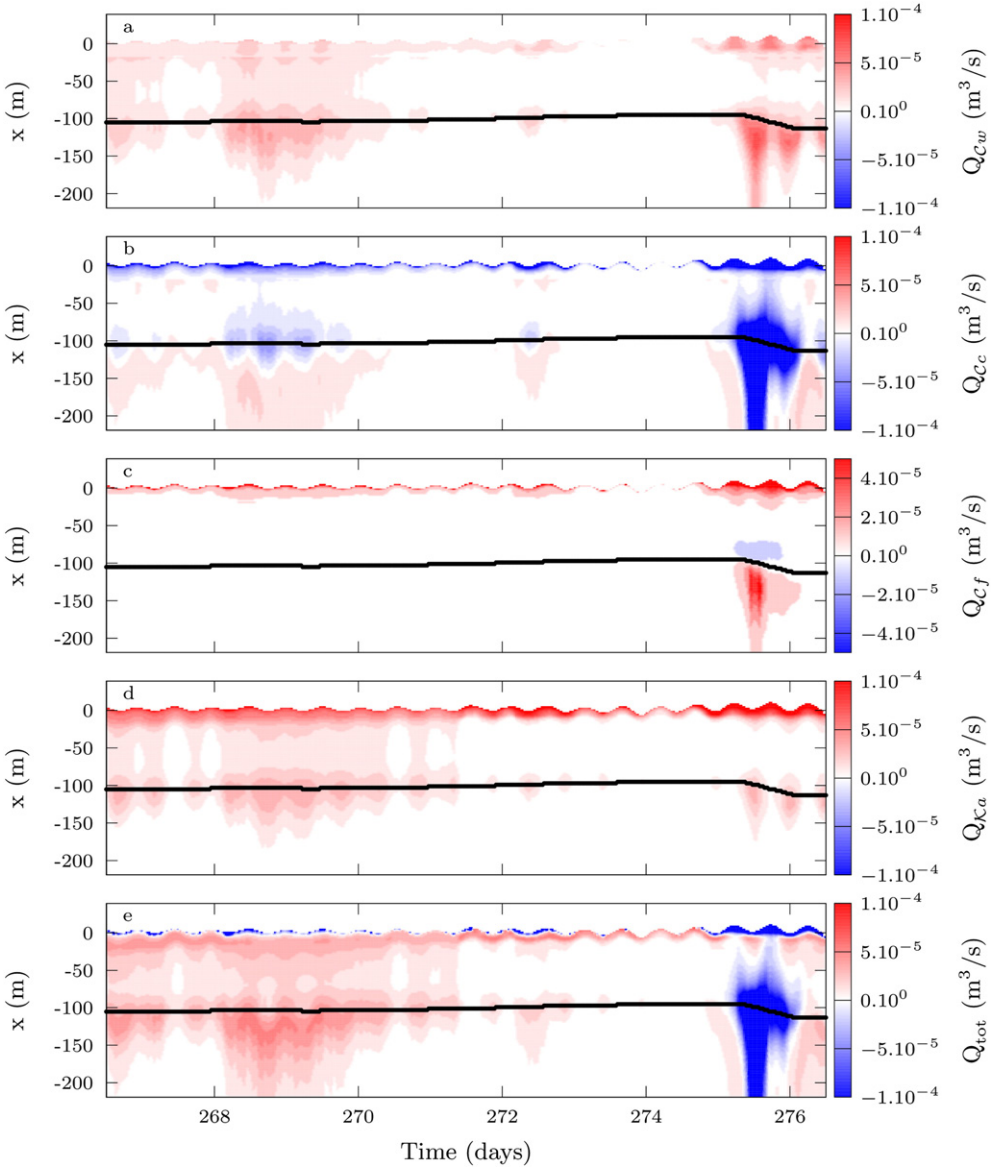

Fig. 8. Time–space diagram of simulated (a) Q_{Cw} sediment transport mode, (b) Q_{Cc} sediment transport mode, (c) Q_{Cf} sediment transport mode, (d) Q_{Ka} sediment transport mode and (e) total sediment flux for the Duck94 experiment. Superimposed dark line indicates the simulated sandbar crest positions.

experiments. This inter-site variability suggests that the physical processes governing beach profile dynamics are still not entirely taken into account with our approach. The large variations in the model parameters from one site to another are the signature of an attempt of the parameters to compensate model errors that primarily arise from simplifications and misspecification of the physics. This statement is not specific to our model but to all existing beach profile models that systematically need calibration from one site (or experiment) to another (e.g., Plant et al., 2004; Ruessink et al., 2007). Among the misspecification of the physics, which are common to other phase-averaged beach profile models, ignoring breaking induced turbulence that enhances sediment stirring (Grasso et al., 2012) or sediment transport related to long-wave processes (Roelvink and Stive, 1989; Reniers et al., 2006) can be a source of large errors.

The optimization method provides insightful information on the relative importance of the free model parameters to the ability of the model to match observations. Fig. 9 shows a combination of the normalized deviation of each free parameter from their corresponding best value found at the end of the optimization,

$$\sigma(X) = \frac{|X - X_{\text{best}}|}{X_{\text{best}}} \tag{22}$$

and, the normalized distribution over their relative searching space,

$$D(X) = \frac{X - \overline{(\text{HL}_X - \text{LL}_X)}}{\overline{(\text{HL}_X - \text{LL}_X)}} \tag{23}$$

with HL (LL) standing for the Higher Limit (Lower Limit) of the searching space. By definition, the simulated annealing algorithm is a stochastic process leading to a random behavior of the solution and the associated free parameter combinations. A nearly constant function $\sigma(X)$ of a given parameter X over time indicates the importance of the calibration X to obtain a good model hindcast. Parameters $\mathcal{C}_w$ (Fig. 9b), $\mathcal{C}_c$ (Fig. 9c), and $\mathcal{K}_a$ (Fig. 9e) have relatively

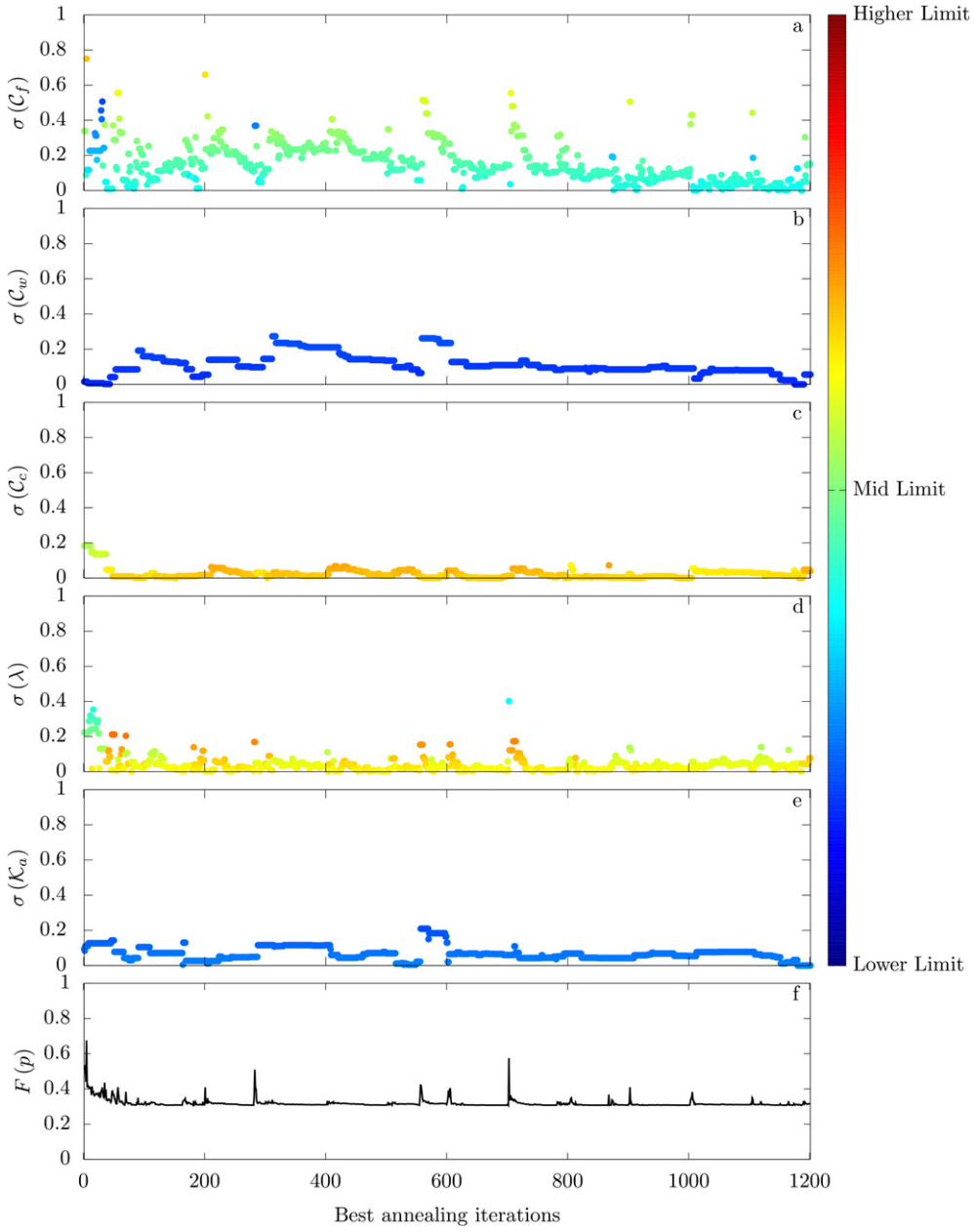

Fig. 9. Evolution of the normalized deviation of each free parameter from their corresponding best-fit value during the optimization process on the Duck94 data-set: (a) $\mathcal{C}_f$, (b) $\mathcal{C}_w$, (c) $\mathcal{C}_c$, (d) λ and (e) $\mathcal{K}_a$. Colors indicate the distribution of each free parameter over their corresponding searching-space. (f) Evolution of the cost function $F(p)$ between model and observation.

constant $\sigma(X)$ and $D(X)$ values over the successive retained trials compared to $\mathcal{C}_f$ (Fig. 9a) and λ (Fig. 9d). This highlights the dominant role of the physical processes associated with these three parameters, the velocity and acceleration skewness and the mean current, with respect to the delay and damping processes. For the Duck82 experiment, the only random trend is found for λ, with $\mathcal{C}_f$ nearly steady through the optimization. The coefficients found for the Duck94 experiment are likely more accurate because of the large range of cross-shore sandbar behaviors implying a more balanced training of each free parameters. The trial values of $\mathcal{C}_w$ and $\mathcal{K}_a$ are found between the mid and lower limits throughout the optimization and converge to the values listed in Table 1. Considering that acceleration skewness is a relevant process for onshore sandbar migration, the optimized $\mathcal{C}_w$ found here is likely more relevant than that obtained through the optimization process excluding acceleration skewness.

5.2. Cross-shore bar migration

Walstra et al. (2012) demonstrate that water level and wave direction above the bar crest are key parameters controlling both the sandbar migration direction and the sandbar amplitude evolution. To further explore the individual effects of each mode of sediment transport on sandbar behavior, we performed 4500 2-day simulations starting from the Duck94 initial profile and forced by constant wave conditions ($H_{rms0} = 1.0$ m, $T_p = 8$ s), using the Duck94 best-fit parameters. Individual sediment transport modes Qc_w, Qk_a, Qc_c and Qc_f are discriminated to address their respective contribution to sandbar migration rates (dX_b/dt) and amplitude variation rates (dA_b/dt) as a function of water level ($h_{x_b} = 1.1$–3.7 m, $\Delta h_{x_b} = 0.1$ m) and wave obliquity ($\theta_{x_b} = 0$–$38°$, $\Delta\theta_{x_b} = 1.2°$). Onshore (Offshore) sandbar migration corresponds to $\partial X_b/\partial t > 0$ ($\partial X_b/\partial t < 0$) and sandbar growth (decay) corresponds to

$\partial A_b/\partial t > 0$ ($\partial A_b/\partial t < 0$). The subscript x_b denotes values estimated at the initial sandbar crest position. Fig. 10 summarizes the results. For each considered transport mode, the 3 others are switched off.

Fig. 10a and b shows the influence of Q_{cw} on sandbar behavior. The growth of the sandbar through Q_{cw} is found with the bar moving onshore (offshore) for $h_{x_b} > (<)$ 2 m. The maximum growth rate of the bar is found for quasi-shore-normal wave incidence and $h_{x_b} \approx 2$ m. The growth rate systematically decreases with increasing angle of wave incidence. For $\theta_{x_b} > 20°$, both dA_b/dt and dX_b/dt decrease because of wave refraction that reduces the wave height above the bar crest. For $h_{x_b} >$

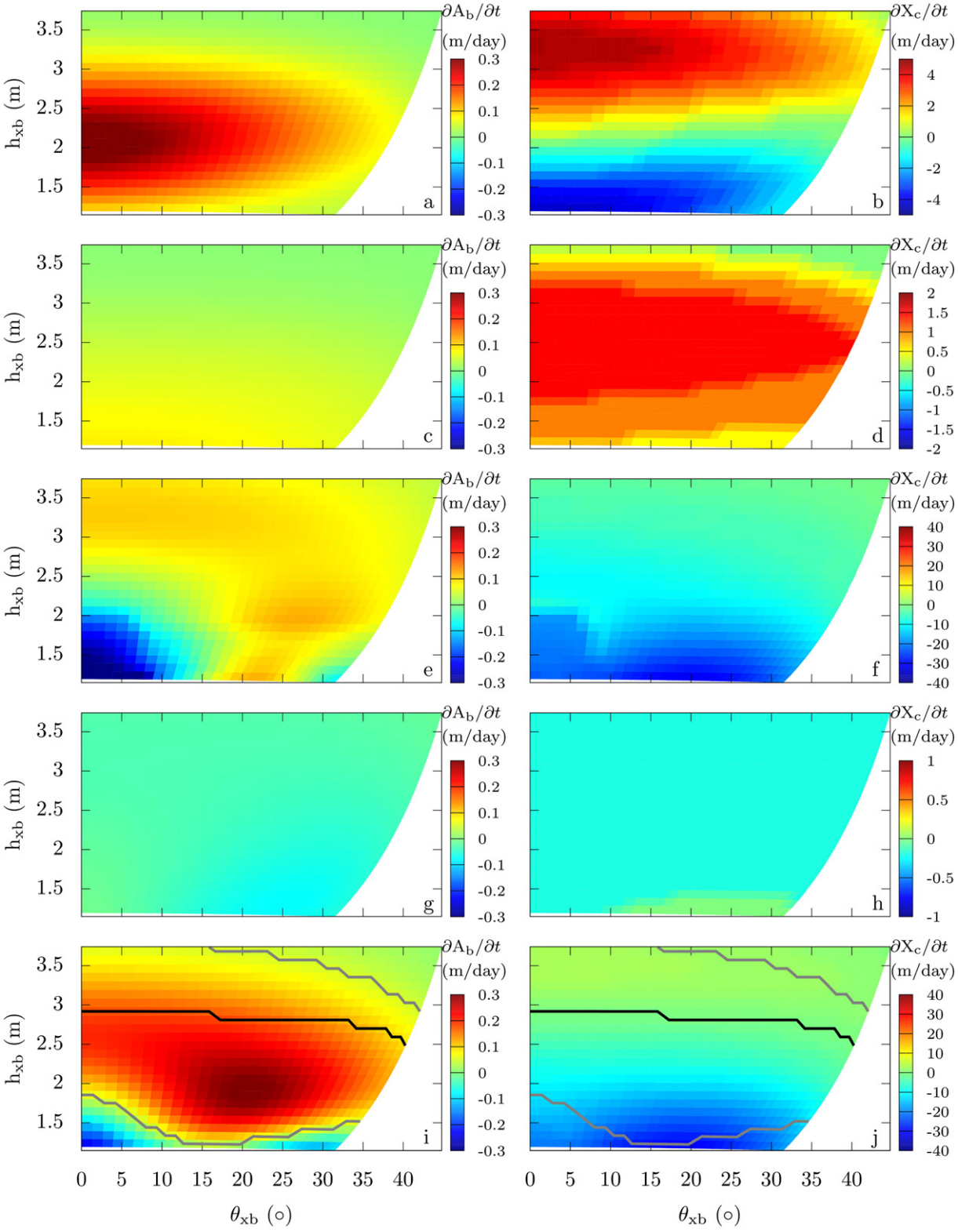

Fig. 10. Predicted sandbar amplitude growth rate (left-hand panels) and cross-shore sandbar migration rate (right-hand panels) as a function of the water depth and angle of wave incidence above the bar crest calculated for each individual sediment transport mode: (a,b) Q_{c_w}, (c,d) Q_{c_a}, (e,f) Q_{c_c}, (g,h) Q_{c_f} and (i,j) total transport Q with the black and grey contour indicating $dX_c/dt = 0$ and $dA_c/dt \leq 0.1$, respectively. In each case, the other 3 modes of transport are switched off. Optimized parameters are identical to the hindcasted Duck94 simulation.

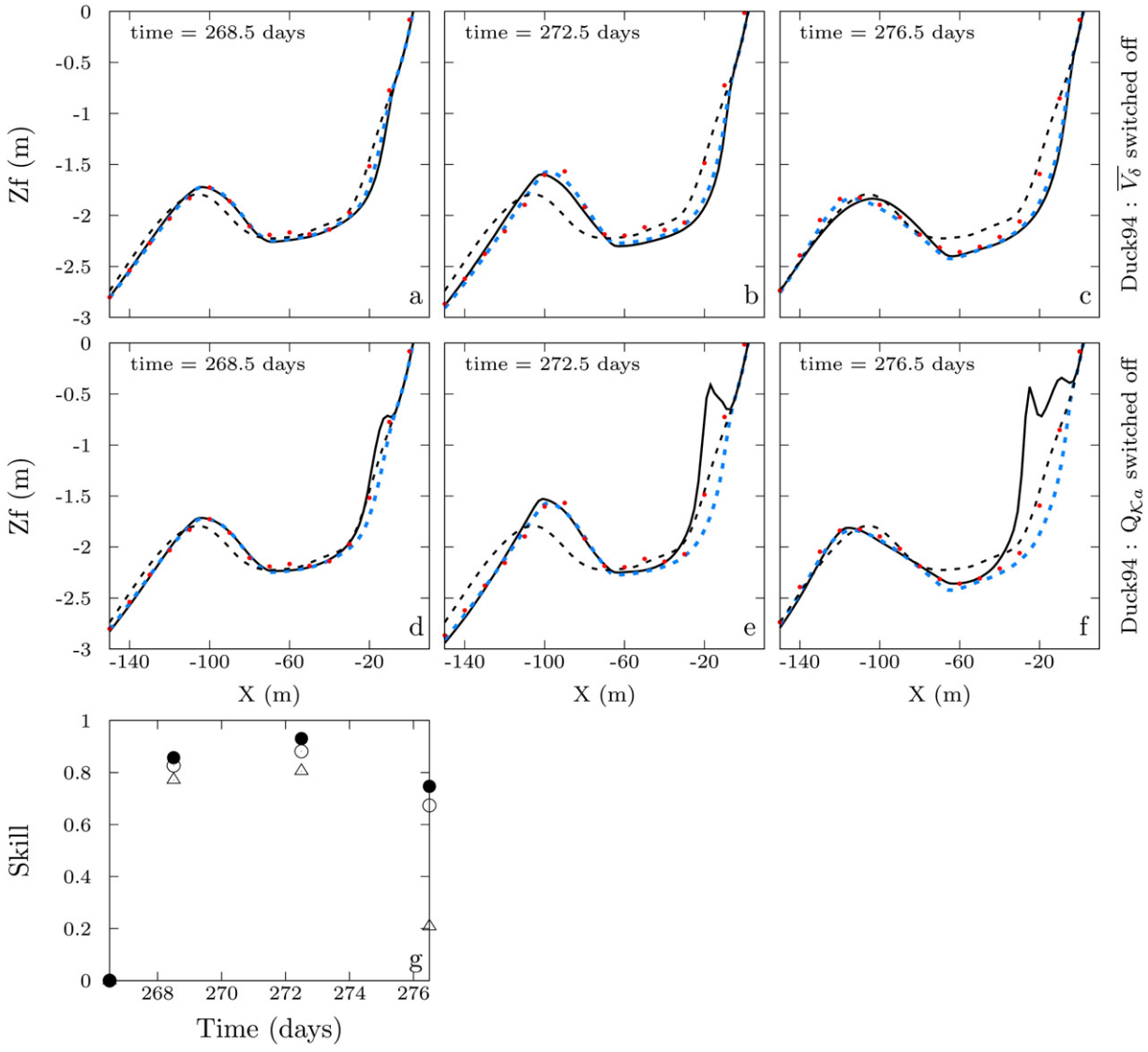

Fig. 11. Comparison between predicted cross-shore bed elevation obtained with all processes included (reference simulation, blue dashed lines) and (a–c) alongshore current switched off ($\overline{V}_\delta = 0$, solid black lines) and (d–f) sediment transport by acceleration skewness switched off ($Q_{\mathcal{K}a} = 0$, solid black lines). The initial profile is represented in dashed black lines and profile observations in red dots. (g) Corresponding prediction quality given by the Brier skill score computed at $-150 \le X \le -50$ m in the active bar zone, with the reference simulation indicated by the filled circles and the simulation with $\overline{V}_\delta$ ($Q_{\mathcal{K}a}$) switched off indicated by the triangles (open circles).

(<) 2.5 m, the sandbar migrates onshore (offshore) with maximum rate obtained for shore-normal wave incidence. For $h_{x_b} > 3.5$ m, the sandbar migrates onshore without any growth. Fig. 10c and d shows the influence of $Q_{\mathcal{K}a}$ on sandbar behavior. For all the $h_{x_b} - \theta_{x_b}$ space, the sandbar is systematically predicted to migrate onshore, although with lower rate than with $Q_{\mathcal{C}w}$. The bar is found to grow very slowly with no clear influence of θ_{x_b}. Maximum migration rates are predicted for a large range of $h_{x_b} - \theta_{x_b}$, with the bar response only weakly sensitive to variations in θ_{x_b}. Accordingly, sediment transport driven by acceleration skewness essentially induces onshore sandbar migration with only little growth, which is mostly modulated by the local water depth on the bar. Fig. 10e and f shows the influence of $Q_{\mathcal{C}c}$ on sandbar behavior. Only a few combinations of h_{x_b} and θ_{x_b} ($h_{x_b} < 2.5$ m and all $\theta_{x_b} < 15^\circ$) result in offshore bar migration with amplitude decay. The maximum sandbar growth occurs for $15^\circ < \theta_{x_b} < 25^\circ$ and $h_{x_b} < 2$ m. For larger angle of wave incidence, the profile evolves from a bar to a terrace profile, with therefore a decay in bar amplitude. Unlike $Q_{\mathcal{C}w}$ and $Q_{\mathcal{K}a}$, $Q_{\mathcal{C}c}$ drives an offshore migration of the sandbar for all the combinations of h_{x_b} and θ_{x_b}, with maximum migration speeds obtained for both low water level and high wave obliquity. Fig. 10g and h shows the influence of $Q_{\mathcal{C}f}$. As expected, this transport mode related to a slope effect mostly acts as a damping term without any significant sandbar migration. $dA_b/dt < 0$ is found for all the combinations of h_{x_b} and θ_{x_b}, with the maximum rate of decay for $h_{x_b} < 2$ m and $\theta_{x_b} > 20^\circ$.

Fig. 10i and j shows the sandbar dynamics associated with the total transport. Importantly, it is different from what is obtained by summing the separate contributions of each transport mode described above, because of the non-linearities involved in the sediment mass conservation Eq. (16). Although addressing a single wave forcing, all the four possible bar evolutions described by Walstra et al. (2012) are simulated despite the more confined $h_{x_b} - \theta_{x_b}$ space. As here we use a different beach profile to that in Walstra et al. (2012), an in-depth inter-comparison of sandbar behavior is not possible. Yet, in our simulations the variability in sandbar behavior appears more sensitive to water level than wave angle. For instance, the model predicts an on/offshore migration threshold around $h_{x_b} \approx 3$m. Overall, wave obliquity regulates the rates of bar growth and migration but does not drive a change from onshore–offshore or decay-growth behavior, except in shallow water ($h_{x_b} < 2$).

Interestingly enough, dA_b/dt and dX_c/dt are very similar in pattern when addressing the total transport (Fig. 10i,j) and the isolated contribution of $Q_{\mathcal{C}c}$ (Fig. 10e,f), implying that mean-current induced sediment transport is the most important contribution for sandbar evolution in shallow water. Additional simulations (not shown) show that (1) the bar decay region moves towards larger water depth with increasing wave height and (2) the bar growth region moves towards lower water depth with increasing wave period, the latter was not addressed in Walstra et al. (2012). Increasing wave height or wave period results in similar bar migration pattern with larger migration rates.

Inclusion of the alongshore current is crucial to predict the observed offshore sandbar migration during the Duck94 field experiment. Running the same simulation as in Fig. 4, but switching off the alongshore current (not shown), shows similar profile evolutions before the onset of energetic waves. This is not surprising as it consists of a period with weakly to non-breaking, rather shore-normal, waves resulting in a weak longshore current. Subsequently, for obliquely incident high-energy waves, the bar further slowly migrates onshore if the longshore current is switched off, in contrast to the observed rapid offshore migration. Because the poor performance of a model without a given process is a strong indication that this process actually provides a meaningful and significant contribution to the morphological evolution, one must re-calibrate the model with the relevant process being excluded to test its importance. Accordingly, to further emphasize the important role of the longshore current in offshore sandbar migration, we performed a new model optimization over the same searching space and trial numbers excluding the contribution of the longshore current. The resulting best-fit model coefficients and resulting beach profile evolutions are shown in Table 1 and Fig. 11a–c, respectively. The model clearly struggles to reproduce the offshore migration in comparison with the simulation including the contribution of the longshore current (Fig. 11c), with skill dropping to 0.2 at the end of the simulation. To minimize the model-observations error, $\mathcal{C}_w$ is strongly decreased to enhance offshore migration. This demonstrates the crucial role of the longshore current during moderate event in moving sandbar offshore.

Because the morphological evolution of a shallow sandbar is likely influenced by acceleration–skewness-induced sediment transport (see Fig. 10c–d), the same approach was performed for the role of acceleration skewness (Fig. 11e–f). By switching off the transport mode $Q_{\mathcal{K}_a}$ only, we notice a small drop in skill at the end of the onshore sequence ($t = 272.5$ days) reflecting the small difference ($\approx 4 - 6$ m) between the two simulated sandbar crest positions (Fig. 11e). However, $Q_{\mathcal{K}_a}$ is important to onshore sandbar migration considering that only a small cumulative time of combined wave and water level conditions promotes large acceleration skewness ($A_s < -0.6$) over the sandbar (see for instance Fig. 2b). C_w increases by a factor 3 to compensate the absence of acceleration-induced sediment transport (see Table 1), which further highlights the importance of acceleration–skewness induced sediment transport in the onshore migration of a shallow sandbar. Ignoring $Q_{\mathcal{K}_a}$ and therefore overestimating the role of velocity–skewness induced sediment transport result in large gradients in sediment flux in the inner surf zone that drive the formation of unrealistic spikes (Fig. 11f).

The skill index indicates that the best model performance is obtained when all the processes are included, with a strongly decreased model skill when excluding the contribution of the longshore current and acceleration skewness (Fig. 11g). Those simulations suggest that including sediment transport driven by acceleration skewness in beach profile model is a necessary requirement to accurately reproduce the behavior of shallow sandbars, in line with Dubarbier et al. (2013) when applying the model to laboratory experiment.

6. Conclusions

A coupled wave–current–sediment transport beach profile model is presented. The model is capable of simulating cross-shore sandbar evolution on the timescales from days to months comprising both rapid offshore and slow onshore migrations. The dominant hydrodynamic processes governing cross-shore sandbar behavior have been discriminated using four modes of sediment transport driven by wave skewness and asymmetry, mean current and slope effects. Acceleration–skewness-induced transport systematically results in a slow onshore sandbar migration together with a slow bar growth. Velocity–skewness-induced transport can drive onshore and offshore bar migrations with substantially larger rates. Mean-current-induced sediment transport systematically drives an offshore bar migration with either bar growth or decay. Slope effects essentially act as a damping term. The water level above the sandbar crest mainly influences the sandbar migration direction while wave obliquity regulates the magnitude of the migration rates and is crucial to accurately simulate offshore sandbar migration during high-energy waves. Including acceleration skewness is a necessary requirement to accurately reproduce the onshore migration of shallow sandbars. Despite the good model profile hindcast, detailed inter-site comparison of best-fit model parameters shows large differences meaning that free parameters can compensate for missing physics. For instance, similar skill could be obtained without acceleration skewness, but by adjusting a parameter in the transport induced by velocity skewness. A next important step will be to implement these cross-shore sediment transport parameterizations into a 2DH morphodynamic model (e.g. Garnier et al., 2008; Castelle and Ruessink, 2011) to further explore the role of cross-shore processes in both up-state and down-state transitions (Michallet et al., 2013).

Acknowledgments

This work was done within the framework of the project BARBEC (ANR N2010 JCJC 602 01). Computer time for this study was provided by the computing facilities MCIA (Mésocentre de Calcul Intensif Aquitain) of the Université de Bordeaux and of the Université de Pau et des Pays de l'Adour. G R acknowledges funding by the Netherlands Organisation for Scientific Research (NWO) under contract 818.01.00g.

References

Abreu, T., Silva, P.A., Sancho, F., Temperville, A., 2010. Analytical approximate wave form for asymmetric waves. Coast. Eng. 57, 656–667.
Bailard, J.A., 1981. An energetics total load sediment transport model for a plane beach. J. Geophys. Res. 86 (C11), 10938–10954.
Baldock, T.E., Holmes, P., Bunker, S., Van Weert, P., 1998. Crossshore hydrodynamics within an unsaturated surf zone. Coast. Eng. 34, 173–196.
Battjes, J.A., Stive, M.J.F., 1985. Calibration and verification of a dissipation model for random breaking waves. J. Geophys. Res. 90 (C5), 9159–9167.
Bertsimas, D., Tsitsiklis, J., 1993. Simulated annealing. Stat. Sci. 8, 10–15.
Birrien, F., Castelle, B., Marieu, V., Dubarbier, B., 2013. On a data-model assimilation method to inverse wave-dominated beach bathymetry using heterogeneous video-derived observations. Ocean Eng. 73, 126–138.
Castelle, B., Ruessink, B.G., 2011. Modeling formation and subsequent nonlinear evolution of rip channels: time-varying versus time-invariant wave forcing. J. Geophys. Res. 116 (F04008). http://dx.doi.org/10.1029/2011JF001997.
Dally, W.R., Brown, C.A., 1995. A modeling investigation of the breaking wave roller with application to cross-shore currents. J. Geophys. Res. 100, 24873–24883.
De Vriend, H.J., Stive, M.J.F., 1987. Quasi-3d modelling of nearshore currents. Coast. Eng. 11, 565–601.
Dubarbier, B., Castelle, B., Marieu, V., Michallet, H., Grasso, F., 2013. Numerical simulation starting from equilibrium to dynamic barred beach profile sequence: application on legi flume experiments. Proc. of Coastal Dynamics 2013. SHOM, France, pp. 129–130.
Elgar, S., Gallagher, E.L., Guza, R.T., 2001. Nearshore sandbar migration. J. Geophys. Res. 106, 11623–11627.
Gallagher, E.L., Elgar, S., Guza, R.T., 1998. Observations of sand bar evolution on a natural beach. J. Geophys. Res. 103, 3203–3215.
Garcez-Faria, A., Thornton, E., Lippmann, T., Stanton, T., 2000. Undertow over a barred beach. J. Geophys. Res. 105, 16999–17010.
Garnier, R., Calvete, D., Falqués, A., Dodd, N., 2008. Modelling the formation and the long-term behavior of rip channel systems from the deformation of a longshore bar. J. Geophys. Res. 113 (C07053). http://dx.doi.org/10.1029/2007JC004632.
Grasso, F., Castelle, B., Ruessink, B.G., 2012. Turbulence dissipation under breaking waves and bores in a natural surf zone. Cont. Shelf Res. 43, 133–141.
Henderson, S.M., Allen, J.S., Newberger, P.A., 2004. Nearshore sandbar migration predicted by an eddy-diffusive boundary layer model. J. Geophys. Res. 109 (C06024). http://dx.doi.org/10.1029/2003JC002137.

Hoefel, F., Elgar, S., 2003. Wave-induced sediment transport and sandbar migration. Science 299, 1885–1887.
Hsu, T.J., Elgar, S., Guza, R.T., 2006. Wave-induced sediment transport and onshore sandbar migration. Coast. Eng. 53, 817–824.
Kuriyama, Y., 2009. Numerical model for bar migration at Hasaki, Japan. Coastal Dynamics.
Kuriyama, Y., 2012. Process-based one-dimensional model for cyclic longshore bar evolution. Coast. Eng. 62, 48–61.
Lippmann, T.C., Holman, R.A., 1990. The spatial and temporal variability of sand bar. J. Geophys. Res. 95 (C7), 11575–11590.
Marieu, V., Bonneton, P., Foster, D.L., Ardhuin, F., 2008. Modeling of vortex ripple morphodynamics. J. Geophys. Res. 113 (C09007). http://dx.doi.org/10.1029/2007JC004659.
Masselink, G., Austin, M., Tinker, J., O'Hare, T., Russell, P., 2008. Cross-shore sediment transport and morphological response on a macrotidal beach with intertidal bar morphology, Truc Vert, France. Mar. Geol. 251, 141–155.
Michallet, H., Castelle, B., Barthélemy, E., Berni, C., Bonneton, P., 2013. Physical modeling of three-dimensional intermediate beach morphodynamics. J. Geophys. Res. 118, 1–15. http://dx.doi.org/10.1002/jgrf.20078.
Nairn, R.B., Roelvink, J.A., Southgate, H.N., 1990. Transition zone width and implications for modelling surfzone hydrodynamics. Proc. 22nd International Conference on Coastal Engineering, ASCE, pp. 68–91.
Pape, L., Ruessink, B.G., Wiering, M.A., Turner, I.L., 2007. Recurrent neural network modeling of nearshore sandbar behavior. Neural Netw. 20, 509–518.
Pape, L., Kuriyama, Y., Ruessink, B.G., 2010a. Models and scales for cross-shore sandbar migration. J. Geophys. Res. 115 (F03043). http://dx.doi.org/10.1029/2009JF001644.
Pape, L., Plant, N.G., Ruessink, B.G., 2010b. On cross-shore migration and equilibrium states of nearshore sandbars. J. Geophys. Res. 115 (F03008). http://dx.doi.org/10.1029/2009JF001501.
Plant, N.G., Holman, R.A., Freilich, M.H., 1999. A simple model for interannual sandbar behavior. J. Geophys. Res. 104, 15755–15776.
Plant, D.G., Holland, K.T., Puleo, J.A., 2004. Prediction skill of nearshore profile evolution models. J. Geophys. Res. 109 (C01006). http://dx.doi.org/10.1029/2003JC001995.
Plant, D.G., Holland, K.T., Holman, R.A., 2006. A dynamical attractor governs beach response to storms. J. Geophys. Res. Lett. 33 (L17697). http://dx.doi.org/10.1029/2006GL027105.
Price, T.D., Ruessink, B.G., 2011. State dynamics of a double sandbar system. Cont. Shelf Res. 31, 659–674.
Reniers, A.J.H.M., Roelvink, J.A., Thornton, E.B., 2004a. Morphodynamic modeling of an embayed beach under wave group forcing. J. Geophys. Res. 109 (C01030). http://dx.doi.org/10.1029/2002JC001586.
Reniers, A.J.H.M., Thornton, E., Stanton, T., Roelvink, J., 2004b. Vertical flow structure during sandy duck: observations and modeling. Coast. Eng. 51, 237–260.
Reniers, A.J.H.M., MacMahan, J.H., Thornton, E.B., Stanton, T.P., 2006. Modelling infragravity motions on a rip-channel beach. Coast. Eng. 53, 209–222.
Roelvink, J.A., Stive, M.J.F., 1989. Bar-generating cross-shore flow mechanisms on a beach. J. Geophys. Res. 94, 4785–4800.
Ruessink, B.G., 2005. Calibration of nearshore process models: application of a hybrid genetic algorithm. J. Hydroinf. 7, 135–149.
Ruessink, B.G., van Enckevort, I.M.J., Kingston, K.S., Davidson, M.A., 2000. Analysis of observed two- and three-dimensional nearshore bar behaviour. Mar. Geol. 169, 161–183.
Ruessink, B.G., Miles, J.R., Feddersen, F., Guza, T., Elgar, S., 2001. Modeling the alongshore current on barred beaches. J. Geophys. Res. 106, 22451–22463.
Ruessink, B.G., Walstra, D.J.R., Southgate, H.N., 2003a. Calibration and verification of a parametric wave model on barred beaches. Coast. Eng. 48, 139–149.
Ruessink, B.G., Wijnberg, K.M., Holman, R.A., Kuriyama, Y., van Enckevort, I.M.J., 2003b. Intersite comparison of interannual nearshore bar behavior. J. Geophys. Res. 108. http://dx.doi.org/10.1029/2002JC001505.
Ruessink, B.G., Kuriyama, Y., Reniers, A.J.H.M., Roelvink, J.A., Walstra, J.A., 2007. Modeling cross-shore sandbar behavior on the timescales of weeks. J. Geophys. Res. Earth Surf. 112 (F03010), 1–15. http://dx.doi.org/10.1029/2006JC000730.
Ruessink, B.G., Pape, L., Turner, I.L., 2009. Daily to interannual cross-shore sandbar migration: observation from a multiple sandbar system. Cont. Shelf Res. 29, 1663–1677.
Ruessink, B.G., Ramaekers, G., van Rijn, L.C., 2012. On the parameterization of the free-stream non-linear wave orbital motion in nearshore morphodynamic models. Coast. Eng. 65, 56–63.
Ruggiero, P., Walstra, D.J.R., Gelfenbaum, G., van Ormondt, M., 2009. Seasonal-scale nearshore morphological evolution: field observations and numerical modeling. Coast. Eng. 56, 1153–1172.
Sallenger, A.H., Holman, R.A., Birkemeier, W.A., 1985. Storm induced response of a nearshore bar system. Mar. Geol. 64, 237–257.
Short, A.D., 1979. Three-dimensional beach stage model. J. Geol. 553–571.
Thornton, E.B., Humiston, R.T., Birkemeier, W., 1996. Bar/trough generation on a natural beach. J. Geophys. Res. 101, 12097–12110.
Trowbridge, J., Young, D., 1989. Sand transport by unbroken water waves under sheet flow conditions. J. Geophys. Res. 94, 10971–10991.
Van Enckevort, I.M.J., Ruessink, B.G., 2003. Video observations of nearshore bar behaviour. part 1: alongshore uniform variability. Cont. Shelf Res. 23, 501–512.
Van Maanen, B., de Ruiter, P.J., Coco, G., Bryan, K.R., Ruessink, B.G., 2008. Onshore sandbar migration at tairua beach (new zealand): numerical simulations and field measurements. Mar. Geol. 253, 99–106.
Van Rijn, L.C., Walstra, D.J.R., Grasmeijer, B., Sutherland, J., Pan, S., Sierra, J.P., 2003. The predictability of cross-shore bed evolution of sandy beaches at the time scale of storms and seasons using process-based profile models. Coast. Eng. 47, 295–327.
Walstra, D.J.R., Reniers, A.J.H.M., Ranasinghe, R., Roelvink, J.A., Ruessink, B.G., 2012. On bar growth and decay during interannual net offshore migration. Coast. Eng. 60, 190–200.
Wright, L.D., Short, A.D., 1984. Morphodynamic variability of surf zones and beaches: a synthesis. Mar. Geol. 56, 93–118.